
AUTOMATED CELL STRUCTURE EXTRACTION FOR 3D ELECTRON MICROSCOPY BY DEEP LEARNING

Jin Kousaka¹, Atsuko H. Iwane², Yuichi Togashi^{1,2}

¹Ritsumeikan University, ²RIKEN Center for Biosystems Dynamics Research

ABSTRACT

Modeling the 3D structures of cells and tissues is crucial in biology. Sequential cross-sectional images from electron microscopy provide high-resolution intracellular structure information. Segmentation of complex cell structures remains a laborious manual task for experts, demanding time and effort. This bottleneck in analyzing biological images requires efficient and automated solutions.

This study explores deep learning-based automated segmentation of biological images, enabling accurate reconstruction of the 3D structures of cells and organelles. We constructed an analysis system for the cell images of *Cyanidioschyzon merolae*, a primitive unicellular red algae. This system utilizes sequential cross-sectional images captured by Focused Ion Beam Scanning Electron Microscopes (FIB-SEM). We adopted the U-Net and performed pre-training to identify and segment cell organelles from single-cell images. In addition, we employed the Segmentation Anything Model (SAM) and the 3D watershed algorithm to extract individual 3D images of each cell from large-scale microscope images containing numerous cells. Finally, we applied the pre-trained U-Net to segment each structure within these 3D images. Through this procedure, we could fully automate the creation of 3D cell models.

Our approach would apply to other cell types, and we aim to build a versatile analysis system. We will also explore adopting other deep learning techniques and combinations of image processing methods to further enhance segmentation accuracy.

Keywords Deep learning · FIB-SEM · U-Net · Segmentation Anything Model · 3D images

1 Introduction

Advanced deep learning technology has significantly improved the accuracy and efficiency of general image recognition tasks. However, its application for biological tissue and medical imaging still needs to be improved.

As a demonstration, we analyzed 3D cell images captured using a Focused Ion Beam Scanning Electron Microscope (FIB-SEM). FIB-SEM is primarily used to measure physical properties and evaluate microstructures [1] of solid samples. Recently, it has also been utilized to analyze 3D structures of cells and tissues. The surface of resin-embedded biological samples is repeatedly cut using a gallium ion beam and imaged by Scanning Electron Microscopes. The serial block-face (SBF) image data, i.e., a sequence of cross-sectional images, is reconstructed as a 3D structure.

However, the intricate boundaries separating structures within each slice, low contrast, and significant noise make it challenging to analyze based on brightness. Furthermore, since images taken with an electron microscope are single channel (grayscale), relying on electron beam reflections, the absence of color information further complicates the analysis. In addition, it is also difficult to identify specific cells within a space containing multiple cells and extract their microstructures. As a result, the segmentation of microstructure depends on experts' subjective evaluation and manual techniques, which consume a lot of time. Image data analysis, which automates this process and is more efficient, objective, and quantitative, is expected to contribute to analyzing various 3D biological images. This study aims to fully automate this process, exploring the application of deep learning in the recognition tasks of cultured cell images.

We chose *Cyanidioschyzon merolae* as a model for the automated reconstruction of 3D cell structures using FIB-SEM [2, 3]. *C. merolae* is a primitive unicellular eukaryote belonging to the red algae, with a diameter of approximately

1.5-2.0 μm [4] (Figure 1). This organism has a simple structure with only one organelle of each type: the nucleus, mitochondrion, plastid, and peroxisome [5]. Each organelle is distributed equally to the two daughter cells [6, 7]. The genome of *C. merolae* and the genomes of its mitochondrion and plastid have been completely sequenced [8, 9, 10, 11]. Moreover, it is relatively easy to synchronize the cell division cycles of multiple *C. merolae* cells in culture with the cycle of light [12]. Due to these characteristics, *C. merolae* is regarded as a model organism for investigating the mechanisms of cell division. Cell division in *C. merolae* has been extensively studied using molecular and cell biological approaches. Recent advances in observation techniques have made it possible to observe dynamic changes in each living cell's behavior and target molecules [13]. However, the physical mechanism of division control based on mechanical properties remains unclear.

Therefore, in this study, we propose an automated method for accurately extracting cell and organelle structures during the division process of *C. merolae*. In previous studies, a method for segmenting each structure from *C. merolae* FIB-SEM images using machine learning has already been proposed [14]. However, this method segments structures from each cross-sectional image in the SBF image containing only one cell. Separating cells and backgrounds is still performed manually and is time-consuming. Additionally, the method disregards the sequential contours between cross-section images and has problems in the segmentation of structures at the cell edge. This study proposes a technique to resolve such shortcomings. By using this method, which allows for the automated and rapid acquisition of 3D structures of multiple *C. merolae* cells, we expect to contribute to investigating mechanical characteristics related to cell division in the future.

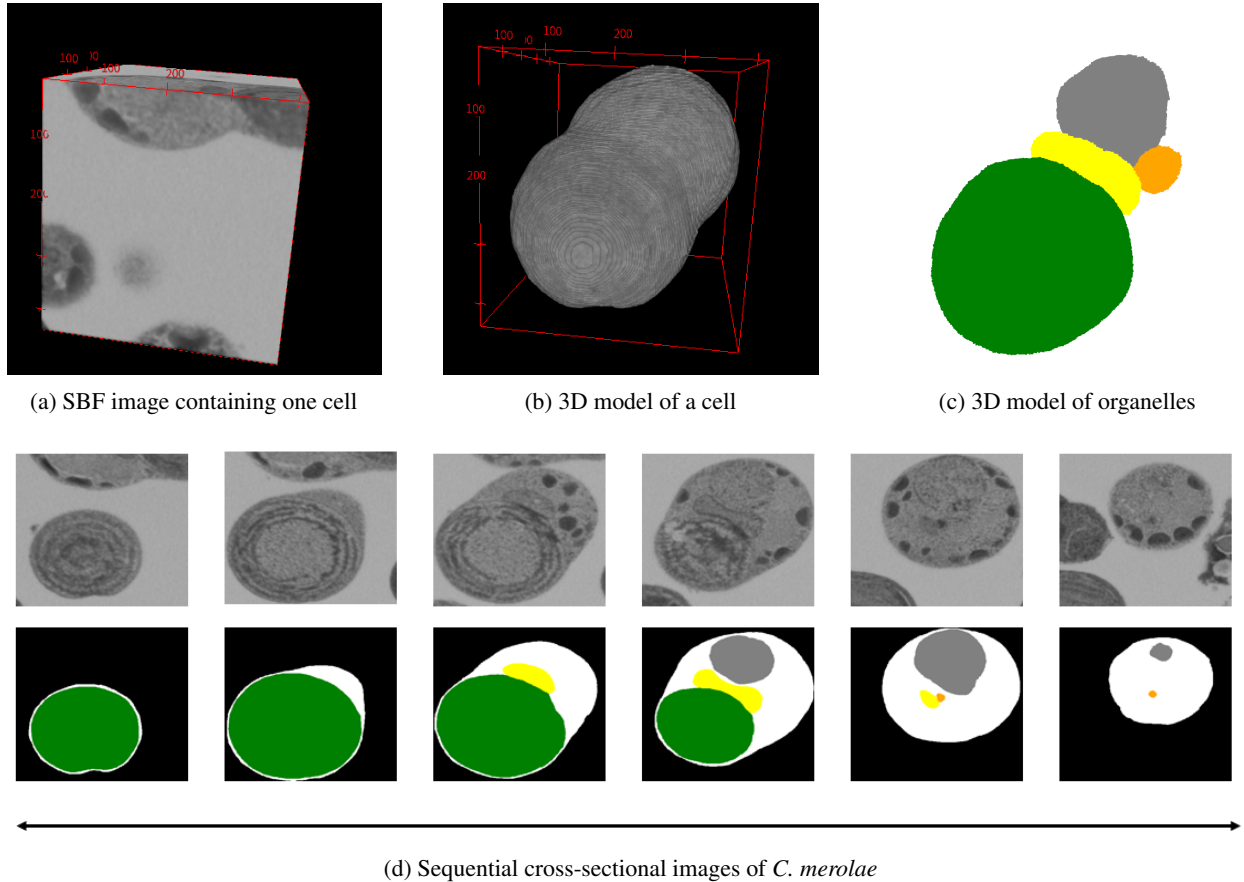


Figure 1: Procedure to reconstruct a 3D model of a cell from sequential cross-sectional images. (a) An SBF image that centrally includes the cell of interest, cropped from FIB-SEM images. (b) By reconstructing this data and removing the background, the 3D model of the cell was produced. (c) The 3D organelle model was visualized by further removing the cytoplasm. Indicating cytoplasm (white), plastid (green), mitochondrion (yellow), nucleus (gray), and peroxisome (orange). (d) This SBF consists of sequential cross-sectional images, as depicted in the top row. Various organelles, the cytoplasm, and the background in these images were manually identified by experts, as shown in the bottom row.

2 Pre-training for Cell Structure Extraction

2.1 Method

2.1.1 Image data acquisition

The images of freeze-fixed samples containing multiple *C. merolae* cells were obtained by FIB-SEM. The obtained sequential sectional images' aspect ratios were corrected, and the noise was removed using a median filter using Amira software (Thermo Fisher Scientific Inc.). Experts cropped to construct learning data images to create an SBF image containing one cell with sides approximately 200-500 pixels long, like Figure 1-(a). They manually segmented each sequential cross-sectional image constituting the SBF image to label plastid, mitochondrion, peroxisome, nuclei, cytoplasm, and background [15]. In other words, all voxels constituting the SBF images were labeled into six classes.

The cell cycle of *C. merolae* is classified into five stages [12], shown as Figure 2. The G1-S phase of the cell cycle is referred to as Stage 1, followed by the G2 phase to the M phase (pre-phase) as Stage 2, the M phase (pre-phase) to the M phase (post-phase) as Stage 3, the M phase (post-phase) as Stage 4, and the M phase (termination phase) as Stage 5. Multiple SBF images were labeled for each stage. The labeled SBF images total 68 and are classified into one of these stages by experts.

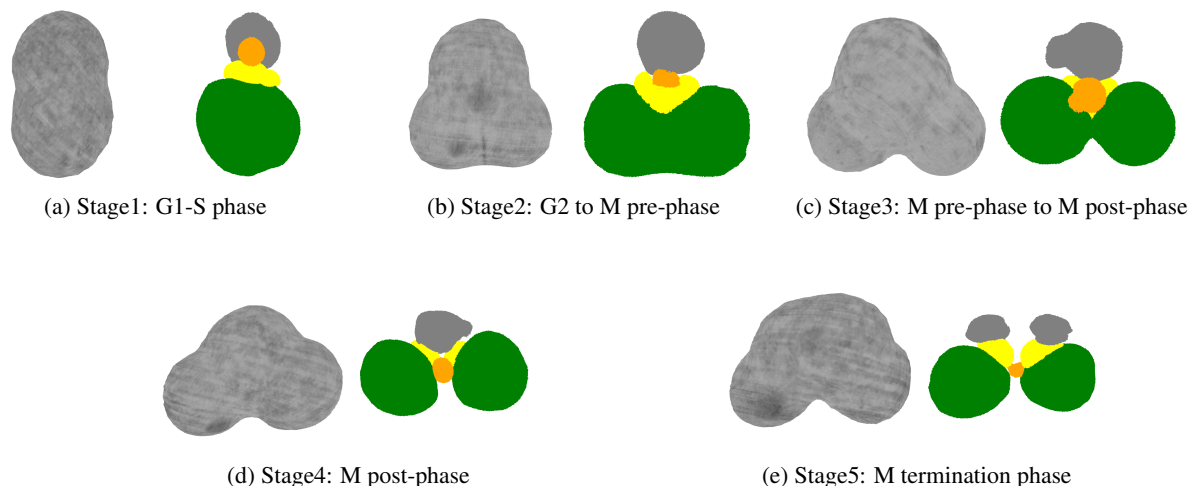


Figure 2: Structural changes associated with the cell cycle of *C. merolae*. Each structure indicates cytoplasm (white), plastid (green), mitochondrion (yellow), nucleus (gray), and peroxisome (orange). Each type of organelle is equally distributed to the daughter cells during division [6, 7]. The division of organelle structures occurs at nearly consistent timings regardless of the individual, although the timing varies depending on the type of organelle [13].

2.1.2 Image data preprocessing

The images obtained by FIB-SEM and the labeled dataset created by experts were preprocessed for deep learning analysis; due to a difference in resolution between the horizontal and vertical directions when capturing images with FIB-SEM, the voxels in the SBF images are shaped as rectangular parallelepipeds rather than cubes. The SBF images were resized using nearest-neighbor interpolation to restore the aspect ratio of the voxels to their actual size ratio, facilitating 3D data analysis. A bilateral filter technique was employed to process the images and remove noise that Amira software could not eliminate [16]. Each sectional image was resized to create cubic voxels, each side measuring 256 pixels, to ensure a consistent input image size for the deep learning model. For effective deep learning, the brightness values of the electron microscope images were normalized to a range of 0 to 1 by dividing by 255. After these preprocessing steps, the dataset was split into different sets for cross-validation, resulting in six cases. In each case, an SBF image was selected as validation data for pre-training the deep learning model, each corresponding to a different stage of cell division. The remaining SBF images were used as training data for the deep-learning model. In addition to the conventional cross-sectional images obtained from the top surface by FIB shaving, the SBF training image dataset was augmented by creating new cross-sectional images from both lateral and anterior views. Details on the number of cells used and the number of cross-sectional images for each dataset in each cross-validation case are presented in Table 1.

2.1.3 Deep neural network architecture

We developed a scanning U-Net neural network model, as illustrated in Figure 3 [17, 18]. Initially created for image segmentation tasks, U-Net is now extensively used in various fields, including medical imaging [19]. The first half of the neural network consists entirely of convolutional layers. On the opposite side, deconvolutional layers gradually restore the image size to the original input. The convolutional and deconvolutional layers are connected by skip connections, designed to prevent information loss due to the encoding of the convolutional layers. In this study, we implemented four stages of convolution and deconvolution, with each deconvolution layer in our model enhanced with an attention gate mechanism [20]. The ReLU function was used as the activation function at each layer, and batch normalization was performed at all layers to prevent overfitting [17, 18]. The U-Net model in this study had approximately one hundred thirty million parameters. We carried out a six-class segmentation task. The input data shape was defined as a tensor of (batch size, number of channels, vertical pixel count of the SBF image, and horizontal pixel count of the SBF image). The label data and the U-Net output values were fed into the TverskyLoss function for loss score calculation [21]. The AdamW learning function was used, with the learning rate starting from a base rate of 0.00001 and decaying by a factor of 0.95 each epoch [22]. The number of epochs was set to 5. All networks were built on a GEFORCE RTX 4090 with 24 GB memory, and the framework was implemented using Python’s TensorFlow. To accelerate learning, the GPU’s tensor cores were automatically utilized.

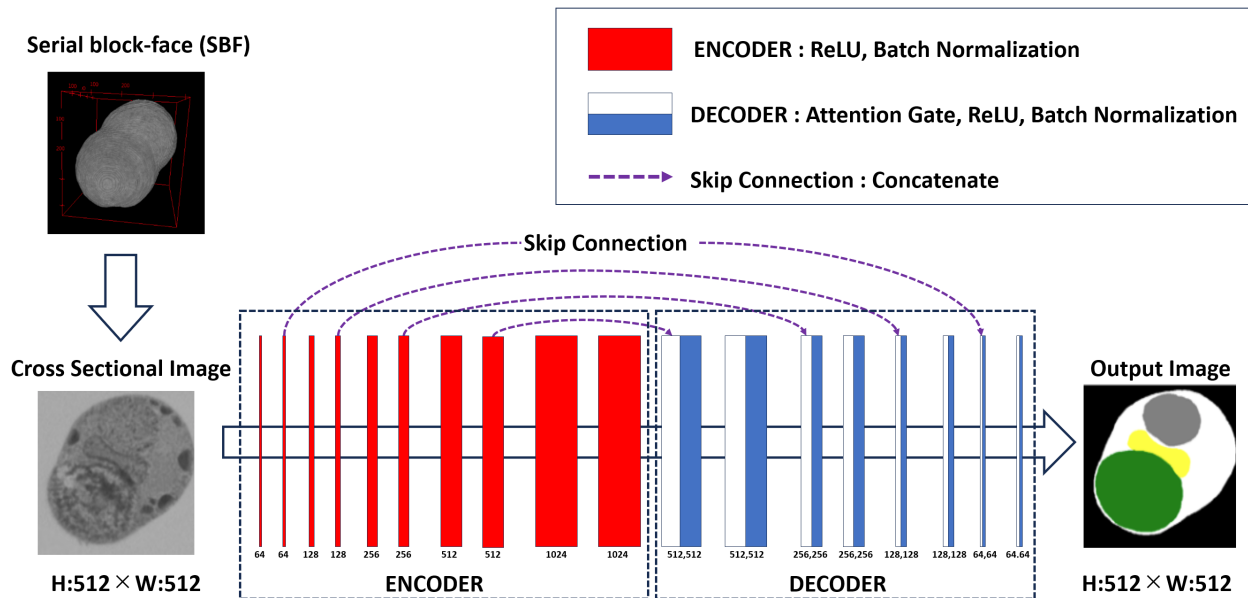


Figure 3: The architecture of U-Net (W and H are output width and height, respectively).

2.1.4 Segmentation accuracy

During the pre-training phase, we evaluated the accuracy of the learning model through cross-validation. In our cross-validation process, we had six distinct cases (Table 1); for each case, a dataset of 63 SBF images was used for training, and a separate set of 5 SBF images (one for each stage in the cell cycle) was used for validation. The validation SBF images did not overlap between cases. Each validation set included one cell from each of the five stages of the cell division cycle. We segmented the sequential cross-sectional images into six classes using the U-Net for each case. The U-Net’s output approached 1 if the segmentation result indicated a specific class and approached 0 otherwise. Finally, we compared these inference results with the label data and evaluated the model using the Intersection over Union (IoU) as Formula (1). The Area of Overlap refers to the intersection area of the predicted and ground truth area. In contrast, the Area of Union refers to the predicted and ground truth together minus the area of overlap.

$$IoU = \frac{\text{Area of Overlap}}{\text{Area of Union}} \quad (1)$$

2.2 Result and discussion

Table 3 presents the IoU score for each case based on the U-Net’s inference results. The table organizes six training classes by row and five cell division stages by column. These results indicate that the average accuracy of background identification is approximately 0.99, suggesting that cells and backgrounds can be identified with very high accuracy, as illustrated in Figure 4. Additionally, the accuracy of plastid inference remains high throughout all stages of cell division. In contrast, mitochondrion and nuclei are smaller in volume than plastid, thus posing a more significant challenge for accurate identification, with an average accuracy of about 0.70. The average accuracy for peroxisomes is notably lower, around 0.45. Furthermore, the inference accuracy for all classes tends to decrease gradually as the cell division stage progresses.

Plastids are more easily identifiable due to their size, unique structure, and distinct brightness values. In contrast, mitochondria and nuclei have brightness values similar to those of background and starch, making them more challenging to identify. Additionally, peroxisomes are assumed to be difficult for deep learning models to learn due to their irregular shapes that vary from cell to cell and brightness values similar to background and starch [23, 24]. Furthermore, as cell division progresses, especially before division, a single SBF image may encompass two cells, increasing the complexity of cell structures within SBF images and potentially decreasing the inference accuracy as cell division advances.

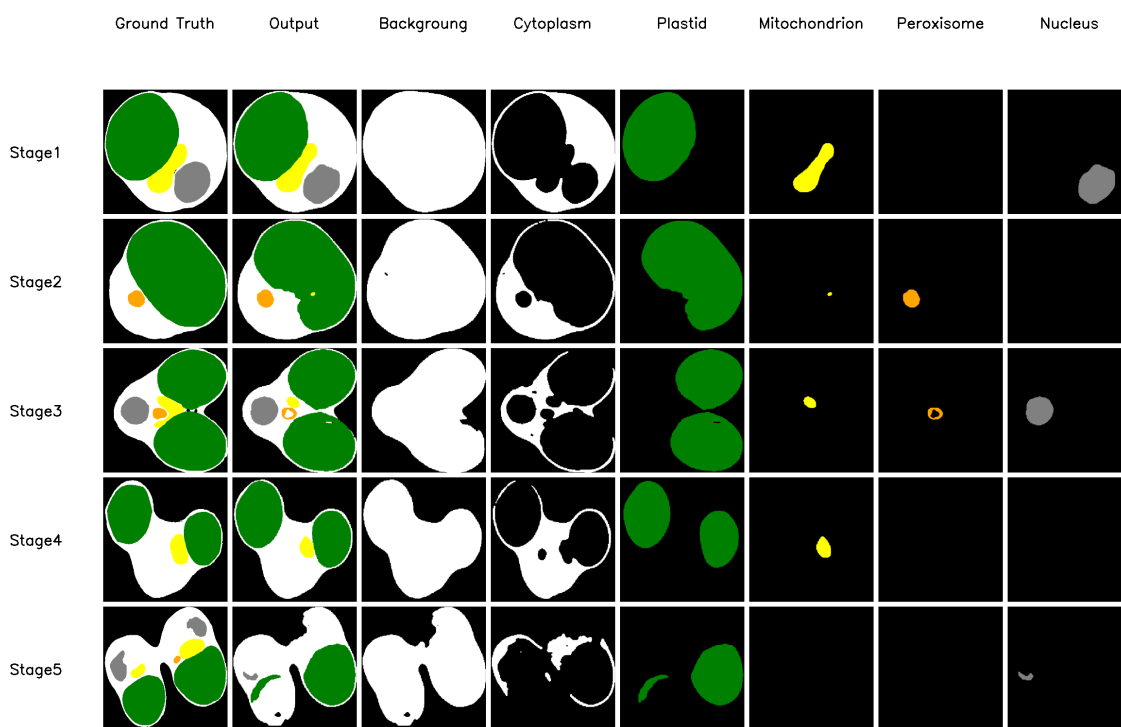
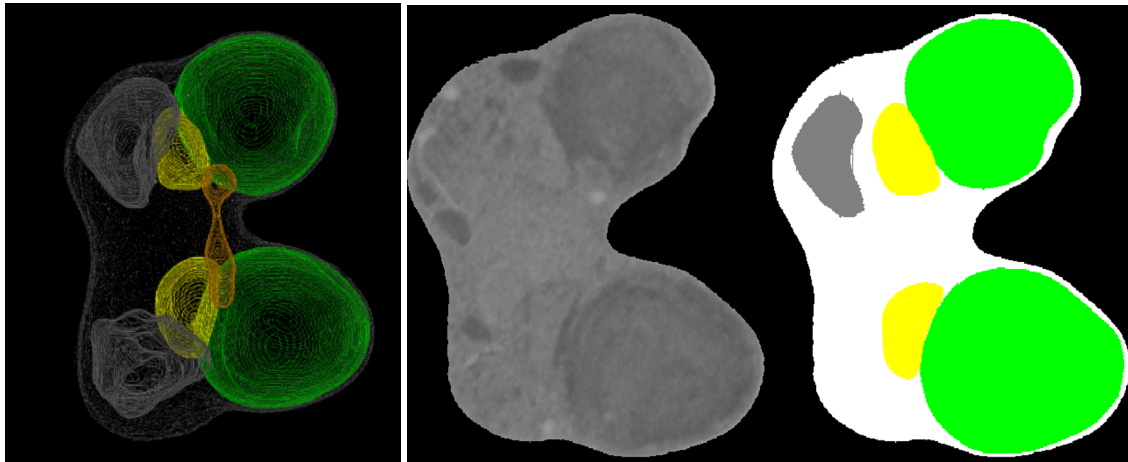


Figure 4: The example illustrating the observation of a 3D cell model from three directions. Inference results for the validation dataset using a model obtained through pre-training. Each structure indicates cytoplasm (white), plastid (green), mitochondrion (yellow), nucleus (gray), and peroxisome (orange). The output images of the plastid and cytoplasm closely match the ground truth.

2.3 Enhancing Segmentation Accuracy

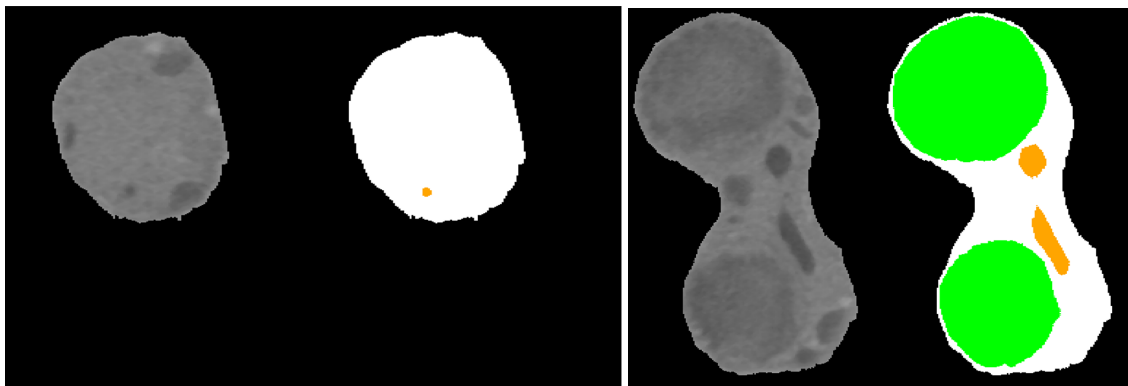
We segmented various cellular organelles from cross-sectional images of 2D pictures. However, a problem was identified with low identification accuracy in some classes. To address this issue, we generated new cross-sectional images perpendicular to the original images, using the 3D SBF data, as shown in figure 5. We used these images for inference with a pre-trained model. This model calculates the probability of belonging to all classes for each voxel (the smallest unit of a 3D image). Three predictive values are obtained for each voxel with inference from three directions. The class with the highest probability is selected when different classes are predicted. This process may introduce noise, so a median filter removes noise after selection. As a result, as shown in table 3, some cases showed no change or a slight decrease in predictive accuracy, but other samples showed a clear improvement in accuracy. This suggests that it might not be possible to accurately determine the class from a cross-sectional image from a specific direction. Also,

considering that the orientation of the cell to be imaged cannot be predetermined and that inference from difficult angles is inevitable, inferring from three directions is worthwhile, even if it means accepting a slight decrease in accuracy.



(a) 3D Model - Captured Direction

(b) Cross-section 1 - Captured image and Label Data



(c) Cross-section 2 - Captured image and Label Data

(d) Cross-section 3 - Captured image and Label Data

Figure 5: Cross-sections and label data of cells in various directions. (a) a 3D cell model reconstructed from captured consecutive cross-sectional images. This model is visualized from the captured direction. (b) includes consecutive cross-sectional images taken near the center of the cell (left) and label data created by experts based on them (right). (c) and (d) display new cross-sectional images generated from stacked consecutive cross-sectional images (left) and the corresponding label data (right). These images were generated from two directions, one aligned with the captured direction and the other perpendicular. Each panel indicates cytoplasm (white), plastid (green), mitochondrion (yellow), nucleus (gray), and peroxisome (orange).

3 Large-Scale Microscopic Image segmentation

3.1 Segmentation Anything Model

In this study, our developed U-Net model utilized sectional images containing a single cell extracted by experts as training data. However, this model is not ideally suited for analyzing images with multiple cells. Therefore, to automate the entire process, it is necessary to develop another method capable of automatically creating images comparable to expert-generated SBFs. To generate SBFs automatically, we initially utilized SAM to distinguish cells and backgrounds automatically. Developed by Meta, the Segmentation Anything Model (SAM) enables easy segmentation of cells and backgrounds from large-scale microscopic images containing multiple cells [25]. SAM has been trained on over 110 million images using over one billion masks and possesses zero-shot capabilities, enabling it to extract structures from unknown classes. Our study employed SAM to extract cells from the background in microscopic images containing

multiple cells. While SAM demonstrated high accuracy in cases with clear cell contours, its performance was less effective in instances where cell contours were less defined, as shown in Figure 6. It presents challenges in extracting cellular organelles from SBFs with indistinct cell outlines. Therefore, although SAM works well for separating cells from backgrounds, a U-Net model trained to recognize cell organelles from SBF images is needed to overcome its limitations in more complex images.

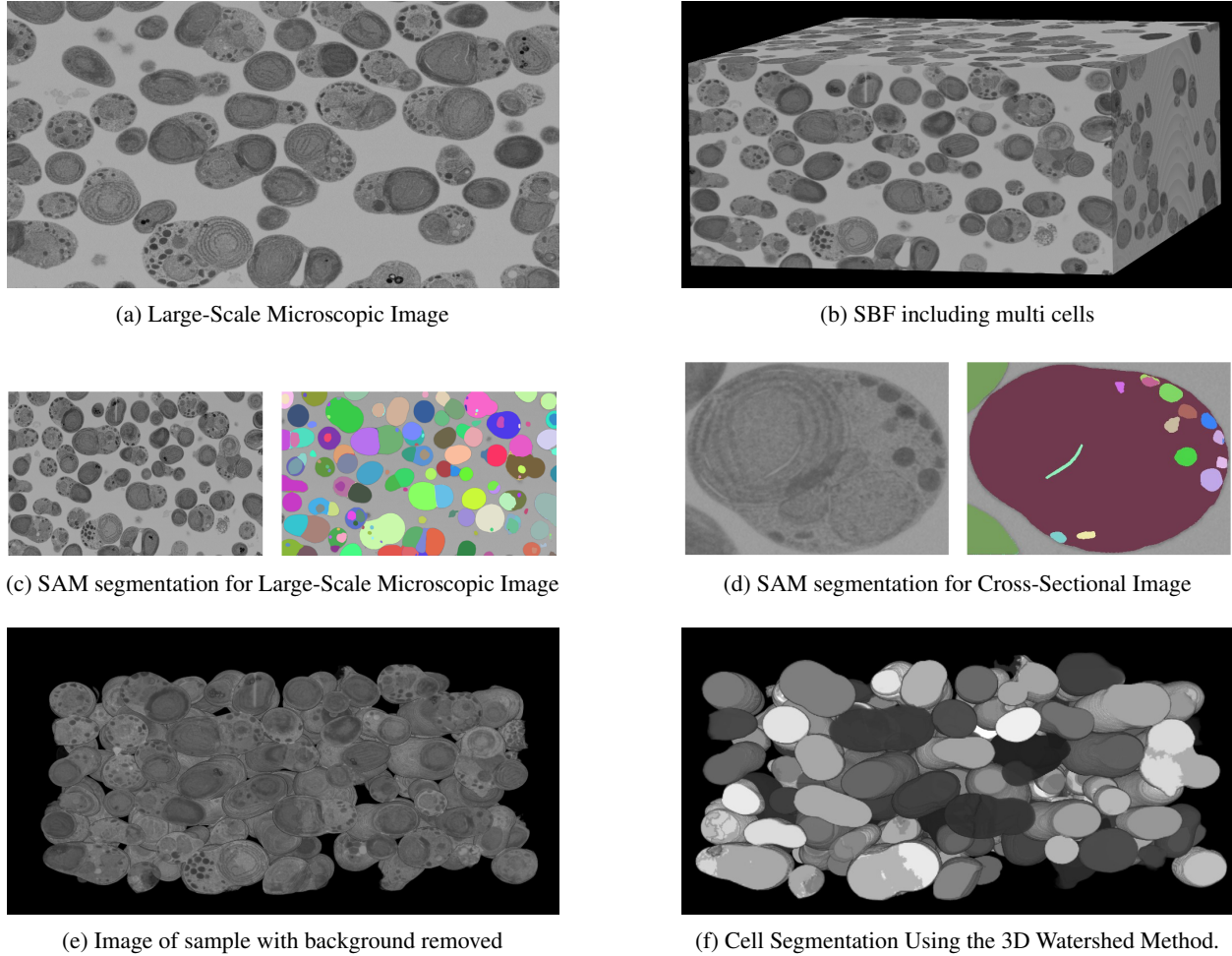


Figure 6: A schematic diagram of automatically identifying individual cells from a 3D image containing multiple cells using SAM and the 3D Watershed Method. (a), (b) Cross-sectional image of a sample containing multiple cells and its SBF. (c) SAM is used to extract cells from the background. (d) SAM is difficult to classify cellular organelles. (e) Background identified by SAM is removed from the SBF in (b). (f) The 3D watershed method identifies and color-codes individual cells.

3.2 3D watershed algorithm

The next challenge was automating individual cell identification after completing the classification between cells and backgrounds using SAM segmentation. For this task, we employed the 3D watershed method. The Watershed algorithm segments image regions based on brightness values [26]. This algorithm simulates water flowing from mountains to valleys, dividing the image into different areas. The 3D watershed algorithm extends this concept to three dimensions, enabling the segmentation of the image space by structural region. This method allows for the identification of structures on a per-cell basis. Typically, images are binarized into black and white before implementing this method, clearly distinguishing between areas of high and low brightness values. A specific brightness threshold is needed for this binarization.

Applying the Watershed method directly to noisy images can be challenging, especially when noise obscures the contours of structures, hindering effective segmentation. To address this, we initially used SAM segmentation for large-scale microscopic images containing multiple cells. This preliminary step facilitated image binarization by distinguishing between cells and background. While SAM operates on 2D images and cannot fully determine the continuity between structures in consecutive images, it significantly aids initial segmentation. Following SAM analysis, we applied the 3D Watershed algorithm for further segmentation, making SAM a supportive tool in the 3D Watershed process.

We used an ImageJ plugin to process the continuous cross-sectional images captured by FIB-SEM and applied the 3D Watershed algorithm. This technique enabled us to identify different cells individually, as shown in Figure 5-f. Thus, the process of creating an SBF image containing a single cell and identifying each cell and cell organelle, previously done manually by experts, has now been fully automated.

4 Discussion

We have successfully established a method to automatically segment and focus on specific cells within a mixed spatial environment in 3D imagery. By incorporating the latest deep learning models, which are being released at an ever-increasing rate, we can further enhance the accuracy of our inferences. This research method was achieved by employing deep learning analysis techniques, which require a substantial amount of high-quality, expertly labeled data as a prerequisite. The necessity for extensive labeled data poses a potential bottleneck for future advancements in this field. This research holds significant promise for biologists, particularly in aiding the morphological and dynamic analysis of cellular and tissue structures in 3D. The ability to automatically segment and analyze intricate cellular compositions in three dimensions provides a powerful tool for biological research.

Tables

Table 1: The dataset used for cross-validation of pre-training. 'Case Number' refers to the consecutive number for each case of cross-validation. The number of cells used for training data in each cell cycle is denoted as 'Cells,' while the number of cross-sectional images used for training is indicated as Learning Images 'LI.' Validation Images 'VI.' represent the number of cross-sectional images used for the validation data.

Case Number	Cell Cycle Stage																	
	Stage1			Stage2			Stage3			Stage4			Stage5			Total		
	Cells	LI	VI	Cells	LI	VI	Cells	LI	VI	Cells	LI	VI	Cells	LI	VI	Cells	LI	VI
1	24	16,568	482	12	15,701	588	11	13,852	426	11	15,098	550	5	7,695	424	63	68,914	2,470
2	24	16,660	470	12	15,520	342	11	13,854	432	11	14,974	580	5	7,327	672	63	68,335	2,496
3	24	16,533	464	12	15,233	514	11	13,798	470	11	15,373	416	5	7,218	800	63	68,155	2,664
4	24	16,696	404	12	15,245	420	11	13,881	362	11	15,537	384	5	7,725	370	63	69,084	1,940
5	24	16,723	340	12	15,185	478	11	13,805	388	11	15,452	440	5	7,748	348	63	68,913	1,994
6	24	16,706	460	12	15,466	376	11	13,927	340	11	15,420	418	5	7,492	374	63	69,011	1,968

Table 2: The scanning 3D U-Net Architecture (K, O, I, D, W, H are kernel size, output channel, input channel, output depth, output width, and output height, respectively).

Network Path	Layer	Size of $K_W \times K_H \times O \times I$	Output Size ($O \times W \times H$)	Attention	Batch Normalization	Activation
Encoder	conv1	$3 \times 3 \times 64 \times 1$	$64 \times 256 \times 256$	False	True	ReLU
	conv2	$3 \times 3 \times 64 \times 64$	$64 \times 256 \times 256$	False	True	ReLU
	conv3	$3 \times 3 \times 128 \times 64$	$128 \times 128 \times 128$	False	True	ReLU
	conv4	$3 \times 3 \times 128 \times 128$	$128 \times 128 \times 128$	False	True	ReLU
	conv5	$3 \times 3 \times 256 \times 128$	$256 \times 64 \times 64$	False	True	ReLU
	conv6	$3 \times 3 \times 256 \times 256$	$256 \times 64 \times 64$	False	True	ReLU
	conv7	$3 \times 3 \times 512 \times 256$	$512 \times 32 \times 32$	False	True	ReLU
	conv8	$3 \times 3 \times 512 \times 512$	$512 \times 32 \times 32$	False	True	ReLU
	conv9	$3 \times 3 \times 1024 \times 512$	$1024 \times 16 \times 16$	False	True	ReLU
	conv10	$3 \times 3 \times 1024 \times 1024$	$1024 \times 16 \times 16$	False	True	ReLU
Decoder	deconv1	$3 \times 3 \times 512 \times 1024$	$512 \times 32 \times 32$	True	True	ReLU
	deconv2	$3 \times 3 \times 512 \times 512$	$512 \times 32 \times 32$	True	True	ReLU
	deconv3	$3 \times 3 \times 256 \times 512$	$256 \times 64 \times 64$	True	True	ReLU
	deconv4	$3 \times 3 \times 256 \times 256$	$256 \times 64 \times 64$	True	True	ReLU
	deconv5	$3 \times 3 \times 128 \times 256$	$128 \times 128 \times 128$	True	True	ReLU
	deconv6	$3 \times 3 \times 128 \times 128$	$128 \times 128 \times 128$	True	True	ReLU
	deconv7	$3 \times 3 \times 64 \times 128$	$64 \times 256 \times 256$	True	True	ReLU
	deconv8	$3 \times 3 \times 64 \times 64$	$64 \times 256 \times 256$	True	True	ReLU
	conv	$1 \times 1 \times 6 \times 64$	$6 \times 256 \times 256$	True	False	SoftMax

Table 3: Inference accuracy of the pre-trained model. Evaluated the inference results of the model for each cellular organelle, in each case of cross-validation and for each stage of the cell cycle, based on four criteria: IoU score.

Stage	1		2		3		4		5	
	1 direction	3 directions	1 directions	3 directions						
Cytoplasm	0.869	0.882	0.790	0.830	0.783	0.806	0.786	0.796	0.778	0.804
Chloroplast	0.954	0.958	0.899	0.928	0.924	0.945	0.937	0.941	0.918	0.944
Mitochondria	0.825	0.857	0.581	0.703	0.712	0.804	0.759	0.754	0.625	0.711
Peroxisome	0.548	0.535	0.516	0.596	0.483	0.601	0.509	0.546	0.148	0.135
Nuclear	0.852	0.883	0.734	0.801	0.705	0.697	0.701	0.696	0.597	0.630
Background	0.996	0.996	0.996	0.996	0.996	0.996	0.997	0.997	0.998	0.998

References

- [1] B. J. Inkson, T. Steer, G. bus, and T. Wagner. Subsurface nanoindentation deformation of Cu-Al multilayers mapped in 3D by focused ion beam microscopy. *J Microsc*, 201(2):256–269, Feb 2001.
- [2] J. Kousaka, A. H. Iwane, and Y. Togashi. A method for automatically constructing 3D cell models from sequential cross-sectional images using deep learning. *Proc. 67th Ann. Conf. ISCIE*, pages 1094–1099, May 2023.
- [3] J. Kousaka, A. H. Iwane, and Y. Togashi. 3D Segmentation and Quantification of Cell Structures by Deep Learning. In *3D Image Conference Proceedings (Web)*, pages P–3, Jul 2023.
- [4] Tsuneyoshi Kuroiwa, Hisayoshi Nozaki, Mtomichi Matsuzaki, Osami Misumi, and Haruko Kuroiwa. Does Cell Size Depend on the Nuclear Genome Size in Ultra-small Algae such as *Cyanidioschyzon merolae* and *Ostreococcus tauri*? *CYTOLOGIA*, 69(1):93–96, 2004.
- [5] S. Y. Miyagishima and K. Tanaka. The Unicellular Red Alga *Cyanidioschyzon merolae*—The Simplest Model of a Photosynthetic Eukaryote. *Plant Cell Physiol*, 62(6):926–941, Sep 2021.
- [6] T. Kuroiwa, H. Kuroiwa, A. Sakai, H. Takahashi, K. Toda, and R. Itoh. The division apparatus of plastids and mitochondria. *Int Rev Cytol*, 181:1–41, 1998.
- [7] O. Misumi, M. Matsuzaki, H. Nozaki, S. Y. Miyagishima, T. Mori, K. Nishida, F. Yagisawa, Y. Yoshida, H. Kuroiwa, and T. Kuroiwa. *Cyanidioschyzon merolae* genome. A tool for facilitating comparable studies on organelle biogenesis in photosynthetic eukaryotes. *Plant Physiol*, 137(2):567–585, Feb 2005.
- [8] N. Ohta, N. Sato, and T. Kuroiwa. Structure and organization of the mitochondrial genome of the unicellular red alga *Cyanidioschyzon merolae* deduced from the complete nucleotide sequence. *Nucleic Acids Res*, 26(22):5190–5198, Nov 1998.
- [9] N. Ohta, M. Matsuzaki, O. Misumi, S. Y. Miyagishima, H. Nozaki, K. Tanaka, T. Shin-I, Y. Kohara, and T. Kuroiwa. Complete Sequence and Analysis of the Plastid Genome of the Unicellular Red Alga *Cyanidioschyzon merolae*. *DNA Res*, 10(2):67–77, Apr 2003.
- [10] M. Matsuzaki, O. Misumi, T. Shin-I, S. Maruyama, M. Takahara, S. Y. Miyagishima, T. Mori, K. Nishida, F. Yagisawa, K. Nishida, Y. Yoshida, Y. Nishimura, S. Nakao, T. Kobayashi, Y. Momoyama, T. Higashiyama, A. Minoda, M. Sano, H. Nomoto, K. Oishi, H. Hayashi, F. Ohta, S. Nishizaka, S. Haga, S. Miura, T. Morishita, Y. Kabeya, K. Terasawa, Y. Suzuki, Y. Ishii, S. Asakawa, H. Takano, N. Ohta, H. Kuroiwa, K. Tanaka, N. Shimizu, S. Sugano, N. Sato, H. Nozaki, N. Ogasawara, Y. Kohara, and T. Kuroiwa. Genome sequence of the ultrasmall unicellular red alga *Cyanidioschyzon merolae* 10D. *Nature*, 428(6983):653–657, Apr 2004.
- [11] H. Nozaki, H. Takano, O. Misumi, K. Terasawa, M. Matsuzaki, S. Maruyama, K. Nishida, F. Yagisawa, Y. Yoshida, T. Fujiwara, S. Takio, K. Tamura, S. J. Chung, S. Nakamura, H. Kuroiwa, K. Tanaka, N. Sato, and T. Kuroiwa. A 100%-complete sequence reveals unusually simple genomic features in the hot-spring red alga *Cyanidioschyzon merolae*. *BMC Biol*, 5:28, Jul 2007.
- [12] K. Suzuki, T. Ehara, T. Osafune, H. Kuroiwa, S. Kawano, and T. Kuroiwa. Behavior of mitochondria, chloroplasts and their nuclei during the mitotic cycle in the ultramicroalga *Cyanidioschyzon merolae*. *Eur J Cell Biol*, 63(2):280–288, Apr 1994.
- [13] T. M. Ichinose and A. H. Iwane. Long-term live cell cycle imaging of single *Cyanidioschyzon merolae* cells. *Protoplasma*, 258(3):651–660, May 2021.
- [14] N. Yudistira, M. Kavitha, T. Itabashi, A. H. Iwane, and T. Kurita. Prediction of Sequential Organelles Localization under Imbalance using A Balanced Deep U-Net. *Sci Rep*, 10(1):2626, Feb 2020.
- [15] Atsuko H. Iwane and K. Ohta. 3D Microstructural Visualization of the Simplest of Eukaryotic Cell (*Cyanidioschyzon Merolae*) during Mitosis Process using Several New Microscopic Techniques. *Biophysical Journal*, 110(3):155a, Feb 2016.
- [16] Francesco Banterle, Massimiliano Corsini, Paolo Cignoni, and Roberto Scopigno. A Low-Memory, Straightforward and Fast Bilateral Filter Through Subsampling in Spatial Domain. *Computer Graphics Forum*, 31(1):19–32, Feb 2012.
- [17] Alex Krizhevsky, Ilya Sutskever, and Geoffrey E Hinton. ImageNet Classification with Deep Convolutional Neural Networks. In *Advances in Neural Information Processing Systems*, volume 25. Curran Associates, Inc., 2012.
- [18] Sergey Ioffe and Christian Szegedy. Batch normalization: Accelerating deep network training by reducing internal covariate shift, 2015.
- [19] Olaf Ronneberger, Philipp Fischer, and Thomas Brox. U-Net: Convolutional Networks for Biomedical Image Segmentation. In *Medical Image Computing and Computer-Assisted Intervention – MICCAI 2015*, pages 234–241, Cham, 2015. Springer International Publishing.

- [20] Ashish Vaswani, Noam Shazeer, Niki Parmar, Jakob Uszkoreit, Llion Jones, Aidan N. Gomez, Lukasz Kaiser, and Illia Polosukhin. Attention is all you need, 2023.
- [21] Nabila Abraham and Naimul Mefraz Khan. A Novel Focal Tversky loss function with improved Attention U-Net for lesion segmentation. *CoRR*, abs/1810.07842, 2018.
- [22] Ilya Loshchilov and Frank Hutter. Fixing Weight Decay Regularization in Adam. *CoRR*, abs/1711.05101, 2017.
- [23] S. Miyagishima, R. Itoh, K. Toda, et al. Microbody proliferation and segregation cycle in the single-microbody alga *Cyanidioschyzon merolae*. *Planta*, 208:326–336, 1999.
- [24] Yuuta Imoto, Kie Itoh, and Yukio Fujiki. Molecular Basis of Mitochondrial and Peroxisomal Division Machineries. *International Journal of Molecular Sciences*, 21(15), 2020.
- [25] Alexander Kirillov, Eric Mintun, Nikhila Ravi, Hanzi Mao, Chloe Rolland, Laura Gustafson, Tete Xiao, Spencer Whitehead, Alexander C. Berg, Wan-Yen Lo, Piotr Dollár, and Ross Girshick. Segment anything, 2023.
- [26] L. Vincent and P. Soille. Watersheds in digital spaces: an efficient algorithm based on immersion simulations. *IEEE Transactions on Pattern Analysis and Machine Intelligence*, 13(6):583–598, 1991.